Correlation between structural and optical properties of CuO/carbon nanoparticle in supports the photocatalytic performance and attenuate the electromagnetic wave

Sultan Ilyas, Heryanto Heryanto, Dahlang Tahir *

Department of Physics, Hasanuddin University, Makassar, 90245, Indonesia

ARTICLE INFO

ABSTRACT

The population increase impacted the increasing demand of the textile industries and electronic devices for supporting daily life. The textile industry uses a toxic chemical at the processing stage, affected by the surface water for disposal without prior treatment. Electronic devices produce a new type of pollution, ex electromagnetic interference (EMI). The multifunction materials against electromagnetic (EM) pollution and radiation of EMI and water pollution treatment are needed. The purposes of this study are to find a correlation between the structural and optical properties of composites CuO-Activated Carbon (CuO-AC) in supports the photocatalyst performance, which analyzing by using X-ray diffraction (XRD), Fourier Transforms Infrared) spectroscopy (FTIR), and Ultraviolet-visible (UV–vis) spectra, respectively. Surface morphology and particle size determined by Transmission Electron Microscopy (TEM). The quantitative analysis of XRD spectra by applying the Scherrer, Williamson-Hall (WH), and Size-Strain Plot (SSP) method using to determine the crystallite size (D), strain (ε), stress (σ), and energy density (u). These parameters are using to identify the monoclinic phase. The optical properties in the form of refractive index (n) and extinction coefficient (k), the dielectric function (ε_1 and ε_2) is determining from the quantitative analysis of FT-IR spectra by applying Kramers–Kronig (K—K) relation. The crystallite size increase, the optical phonon vibration shifted, and close each other's with increasing the amount of AC indicated stable bonding as the effect of the heterogeneous nucleation in the composite. In this study, composite CuO-AC offers an excellent prospect for next bi-functional materials indicated by the degradation up to 87.87 % in 90 min and attenuated 99 % of the electromagnetic wave for 20 % AC.

1. Introduction

A semiconductor material has widely used as a photocatalysis material because of the unique properties that are resistant to corrosion [1–5]. One of the semiconductor materials is Copper (II) oxide (CuO). CuO is one of two stable copper oxide compounds consisting of metal and non-metal [6]. CuO combined with activated carbon (AC) can become an attractive material in various applications due to environmental feasibility and low density for heterogeneous catalysts [6–11].

Photocatalysis from nanomaterials has interesting for scientists in the world [1,2,12–15] due to the unique characteristics such as chemical stability and considerable excitation energy [2,6,14–25]. The structural properties of the nanomaterial have an essential role in supporting the performance of various applications. Recently reported nanoparticle based CuO with and without doping: structural properties of CuO nanostructure [26], nanostructure flower-shaped CuO for photocatalytic and antibacterial [27], nanorods CuO doped by La^{3+} ion [28], Li doped CuO thin film on Si (100) [29], Nanoparticle Li substitute by CuO [30], nanoparticle CuO doped by alkali metals for solar cell application [31], and potassium doped CuO nanostructure [32]. The structural properties such as; the nanoparticle size was analysis by various experimental methods; x-ray diffraction (XRD), transmission electron microscopy (TEM), scanning electron microscopy (SEM), and particle size analyzer (PSA), and also by various analytical models to find the accuracy results between theoretical calculation and the experimental results. The various theoretical model can be used to find the best matching results and for confirmation with the experimental data. The simple calculation model for analyzing the structural properties from the XRD data is the Scherrer, the Williamson-Hall (WH), and the Size-Strain Plot (SSP) model [33,34]. We have successfully applied these models for the

analysis of structural properties of Fe_3O_4 [19], element materials [20], Cu, Cu_2O, and Cu-C [21,33], and composite cement/$BaSO_4$/Fe_3O_4 [22]. These various models used to confirm each other results of the structural properties from the quantitative analysis of XRD spectra and the optical properties analyzed by applying the Kramers-Kronig (K-K) relation in the quantitative analysis of the FT-IR spectra [22,35–38].

In this study, we applied these models for determining the structural properties from the XRD spectra and the K—K relation for determining optical properties from the quantitative analysis of FTIR spectra for CuO and composite CuO-AC (10 % AC and 20 % AC). The XRD and FTIR spectra are from our previous published, which were successfully use for absorber electromagnetic (EM) waves [6]. The crystallite size in our previous study only used the Scherrer methods by considering four high intensity of the diffraction peaks. In this study, we determining the structural parameters including crystallite size by considering all the diffraction peaks for more accurate results by using various models. The structural properties including; crystallite size (*D*), strain (ε), stress (σ), and energy density (*u*) of the material based on the Scherrer method, WH Method and SSP method and the optical properties including; effect of optical phonon vibration based on refractive index (*n*), extinction coefficient (*k*), and dielectric function (ε_1 and ε_2). For our knowledge, there is no reported for the inter-correlation between structural and optical properties to the photocatalytic performance and ability in attenuating the EM wave of the composite CuO-AC. Hence, in this study, we focus on the quantitative analysis of XRD spectra for determining the structural properties from various models and FTIR spectra for determining the electronic and optical properties by applying KK relation. We have included a TEM image to confirm the crystallite size from the quantitative analysis of XRD spectra by various model calculations. For determining the photocatalytic performance of composite CuO-AC, use the UV–vis spectroscopy. The relation between the structural properties, optical properties to the photocatalytic performance, and ability in attenuating the EM wave discussed in detail.

2. Experiment

The experimental of CuO and composites of CuO-activated carbon (CuO-AC) samples were from our previous published paper [6], similar in Ref. [16,18,19]. This study focused on analyzing the XRD spectra and FT-IR spectra of CuO and composites of CuO-AC for 10 % AC and 20 % AC. We use the XRD spectra and FT-IR spectra from our previous published paper in Ref. [6] for advanced analysis in this study. Transmission Electron Microscopy (TEM) image (Hitachi TEM System) to determine the particle size and for photocatalytic performance or liquid waste purifying catalyst by using UV–vis (Ultraviolet-visible) spectroscopy (Shimadzu UV–vis Spectrophotometer UV-1800). The mechanism of photocatalytic performance is following our previously published paper [13] and briefly repeated below.

Methylene blue was used as a model of liquid waste pollutants in photocatalytic performance by using halogen lamps (300 W, OSRAM 645, Germany) as sources of radiation. The sample in the form of a pellet dissolved in 50 mL of methylene blue then measured the absorbance as a control by using UV–vis Spectrometer, then measurement retrieval by applied the radiation and for every 30 min until the solution is clear. The percentage degradation of methylene blue was calculated by using equation; $D\,(\%) = \frac{C_0 - C_t}{C_0} \, x \, 100\%$, where $D\,(\%)$ is the percentage of degradation, C_0 is the control absorbance (before irradiation) and C_t is the absorbance after time *t*.

3. Result and discussion

3.1. Particle size and strain

The quantitative analysis of XRD spectra [6] by WH and SSP calculation used to determine the crystallite size, lattice parameters, volume

lattice, dislocation density, and porosity composite 10 % AC and 20 % AC [19]. Fig. 1 shows the XRD spectra for CuO and composites CuO-AC (10 % AC and 20 % AC) monoclinic structures based on JCPDS: 95−101-1149. For diffraction angles of $20° \leq 2\theta \leq 80°$ confirmed monoclinic structures with diffraction peaks at 32.17°, 35.72°, 38.94°, 48.93°, 53.62°, 58.55°, 61.52°, 66.16°, 68.06°, and 75.20° with *hkl* indices 110, 11$\bar{1}$, 111, 20$\bar{2}$, 020, 202, $\bar{1}$13, 220, 311, and 22$\bar{2}$, respectively. These results from Eq. (1) for monoclinic structures by first calculating the lattice constant (for more detail, see our previous published [6]) and the distance between the atoms in 2 dimensional (*d*) based on the Bragg equation. Crystallite size obtained using the Scherrer equation in Eq. (2), with *k* is 0.94, and the wavelength (λ) of radiation for *Cu Kα* is 1. 54 Å [6,13,16,18,19].

$$\frac{1}{d^2} = \frac{1}{Sin^2\,\beta}\left[\frac{h^2}{a^2} + \frac{k^2\,Sin^2\,\beta}{b^2} + \frac{l^2}{c^2} - \frac{2\,hl\,cos\,\beta}{ac}\right] \quad (1)$$

$$D = \frac{k.\lambda}{\beta.Cos\,\theta} \quad (2)$$

Fig. 1 shows an increase of the full width half maximum (FWHM) for the composite 10 % AC to 20 % AC at the diffraction peaks 32.17°, 35.72°, and 66.16°. The diffraction peaks at 32.17° and 35.72° are due to carbon's influence, similar to previously reported [6,16,17,39]. The diffraction peak at 66.16° is interactions between CuO and AC as the nucleation effect at the site of Cu [19–21]. The C atoms prefer bonding with Cu rather than O atoms, a similar effect for Fe_3O_4 reported in Ref. [13,18,19,34]. In our previous published, we used Scherrer to determine the average crystallite size from the calculation by considering four high intensity of the diffraction peaks. In this study, we determining the crystallite size by considering all the diffraction peaks for more accurate results by plotting relation between $cos\theta$ and $1/\beta$ as can be seen in Fig. 2 for Scherrer model and also continue by WH model in Fig. 3, and SSP model in Fig. 4. By applying the line equation $Y = a*x + b$ [19–25,33] in Figs. 2–4, the slope, and the intercept values are presented in Table 1.

Fig. 3(a)–(c) shows plot data from the WH method consisting of the uniform deformation model (UDM) (Fig. 3(a)), the uniform stress deformation model (USDM) (Fig. 3(b)), and the uniform deformation energy density model (UDEDM) (Fig. 3(c)). WH method is a method of analyzing the of crystallite size (*D*) by considering the ε for UDM, ε, and σ for USDM, and ε, σ, and *u* for UDEDM of the composite which implemented for Fe_3O_4, Cu-C, Cu_2O, composite cement/$BaSO_4$/Fe_3O_4 in our previous published paper in Ref. [19–22,33], and some research results related to the WH method [23–25].
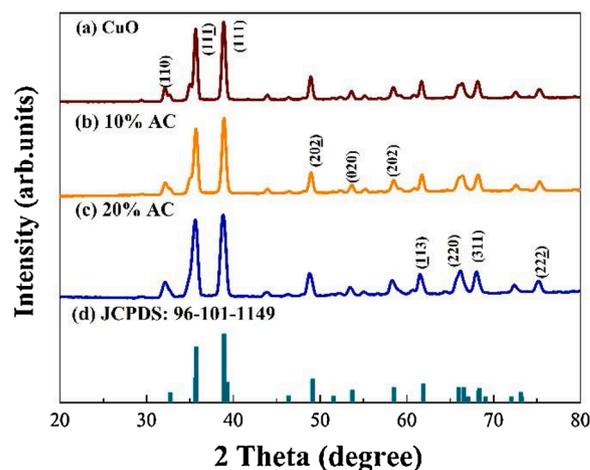
Fig. 1. XRD Spectra with monoclinic phase of CuO and composite CuO-AC (10 % AC and 20 % AC) were taken from Ref. [6] and included JCPDS: 96-101-1149 for comparison.
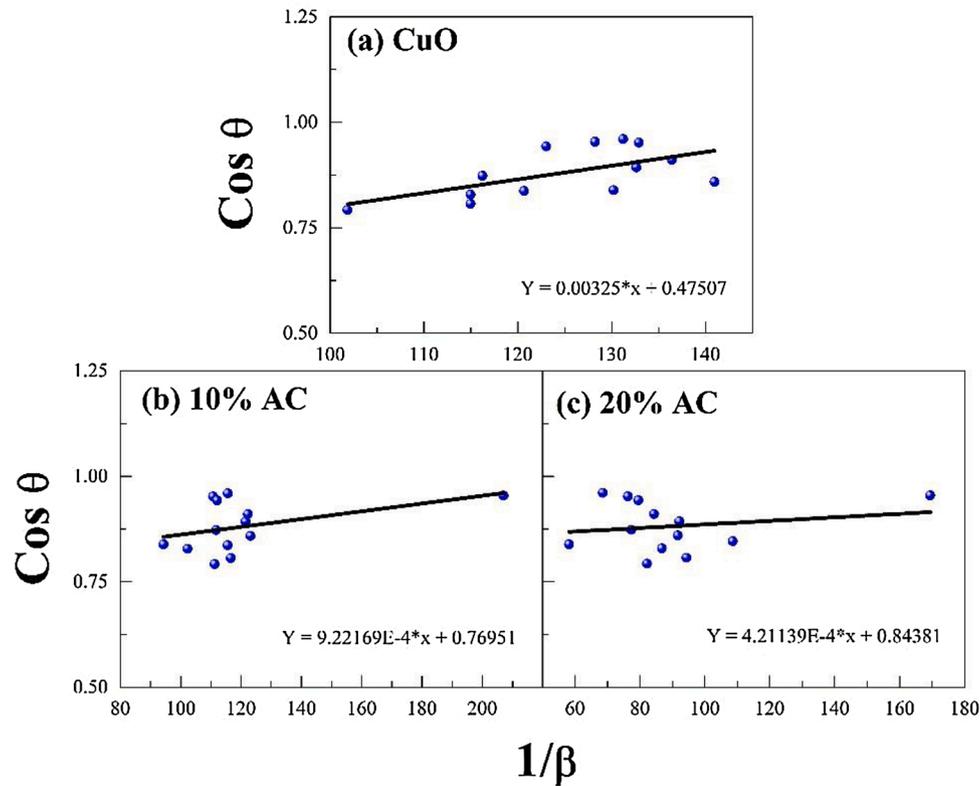
Fig. 2. Scherrer method for CuO and composite CuO-AC (10 % AC and 20 % AC).
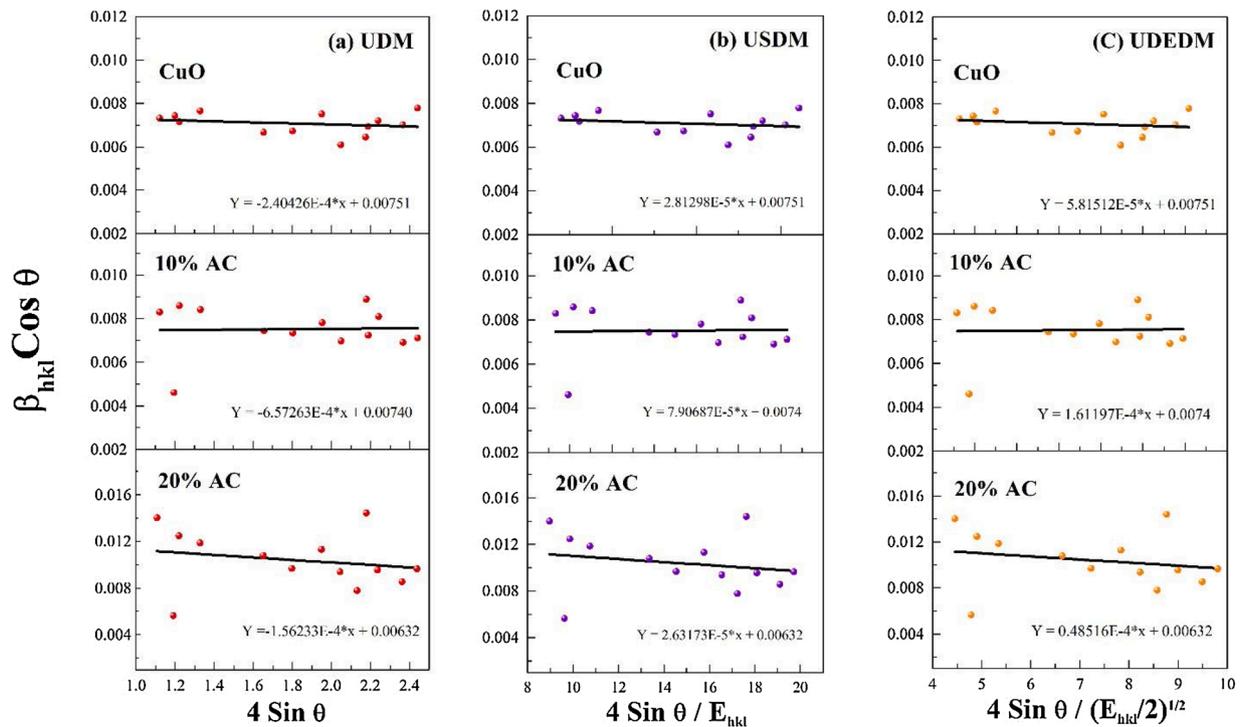
Fig. 3. W-H methods with UDM (a), USDM (b), UDEDM (c) for CuO and composite CuO-AC (10 % AC and 20 % AC).

The UDM model is a model in the WH method by analyzing the crystallite size (D) and strain (ε) of the nanomaterial. The UDM model presented with the slope and the intercept value (see Table 1). Table 2 shows the crystallite size of all models in this study and shows the strain (ε) changes with the addition of AC [6,16,18,19], as can be seen in Fig. 3

(a) shows the interaction between CuO and AC by incorporating two diffraction peaks, consequently increasing the FWHM in the UDM model. The strain (ε) changes with AC addition due to the amorphous AC phase influenced the composite lattice structure [6,19]. Carbon atoms from AC play an essential role in improving the molecules' surface
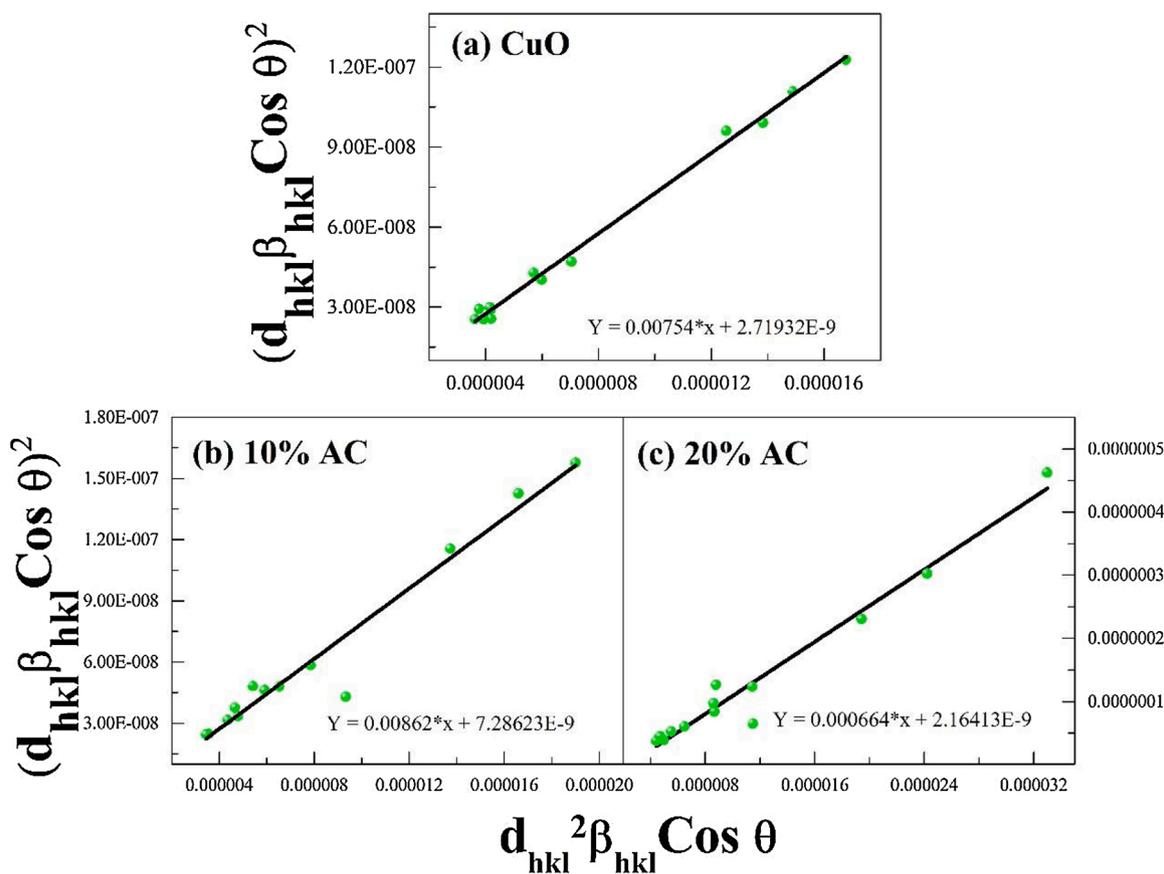
Fig. 4. SSP methods for CuO and composite CuO-AC (10 % AC and 20 % AC).

Table 1
Slope and intercept value of CuO and composite CuO-AC (10 % AC and 20 % AC) base on the Scherrer method (Fig. 2), WH method (UDM (Fig. 3), USDM (Fig. 4), UDEDM (Fig. 5)), and SSP method (Fig. 6).

| Equation | Scherrer Method | Williamson-Hall Method | | | Size-Strain Plot Method |
		UDM	USDM	UDEDM	
Y = a*x + b	$\cos\theta = \dfrac{k.\lambda}{\beta\,D}$	$\beta_{hkl}\cos\theta = \dfrac{k.\lambda}{D} + 4\,\varepsilon\sin\theta$	$\beta_{hkl}\cos\theta = \dfrac{k.\lambda}{D} + \dfrac{4\,\sigma\sin\theta}{E_{hkl}}$	$\beta_{hkl}\cos\theta = \dfrac{k.\lambda}{D} + \left(4\sin\theta\left(\dfrac{2u}{E_{hkl}}\right)^{\frac{1}{2}}\right)$	$(d\beta Cos\theta)^2 = \dfrac{K}{D}\left(d^2\beta Cos\theta\right) + \left(\dfrac{\varepsilon}{2}\right)^2$
Sample	Y	Y	Y	Y	Y
CuO	0.00325*x + 0.47507	−2.40426E-4*x + 0.00751	2.81298E-5*x + 0.00751	5.81512E-5*x + 0.00751	0.00754*x + 2.71932E-9
10 % AC	9.22169E-4*x + 0.76951	−6.57263E-4*x + 0.00740	7.90687E-5*x + 0.00740	1.61197E-4*x + 0.00740	0.00862*x + 7.28623E-9
20 % AC	4.21139E-4*x + 0.84381	−1.56233E-4*x + 0.00632	2.63173E-5*x + 0.00632	0.48516E-4*x + 0.00632	0.00664*x + 2.16413E-9

Table 2
Structural Parameters of CuO and composite CuO-AC (10 % AC and 20 % AC) base on the Scherrer method (Fig. 2), WH method (UDM (Fig. 3), USDM (Fig. 4), UDEDM (Fig. 5)), and SSP method (Fig. 6).

Sample	Scherrer Method	Williamson-Hall Method										Size-Strain Plot Method			
		UDM		USDM			UDEDM								
	D	D	ε	D	ε	σ	D	ε	σ	u		D	ε	σ	u
	(nm)	(nm)	10^{-3}	(nm)	10^{-3}	(Mpa)	(nm)	10^{-3}	(Mpa)	Kjm^{-3}		(nm)	10^{-3}	(Mpa)	Kjm^{-3}
CuO	20.81	20.38	0.24	20.38	0.24	28.13	20.38	0.24	28.13	3.38		25.12	0.11	12.20	0.64
10 % AC	20.60	20.03	0.66	20.03	0.66	79.07	20.03	0.66	79.07	25.98		21.47	0.17	20.54	1.75
20 % AC	21.96	23.01	0.16	23.01	0.16	26.32	23.01	0.16	26.32	2.35		27.29	0.09	11.49	0.53

adsorption energy or charge and active site in bonding together to form heterogeneous nucleation. Homogeneous nucleation may occur at a low concentration of AC and changes to heterogeneous when the amount of AC increases but needs further study to understand the process. AC plays an important role in nucleation, resulting in a new structure with strong bonding formation [6,19–22]. The change of the crystallite size may due to the nucleation indicated that, the structure change as the effect of the photon vibration which is useful for photocatalysist process by transfer their energy to the electron at the atoms.

Fig. 3(b) represents the USDM model in the WH method, which in this model considers the values of *D*, *ε*, and stress (*σ*) of the composite [19–25,33]. The slopes and the intercepts for the USDM model are shown in Tables 1 and 2 for *D*, *ε*, and *σ*. The *D* and *ε* values of the USDM model show the same value as UDM as part of the WH method, and the σ value changes with the addition of AC [6,16,18,19], which explained that by the *σ* of material depends on the values of *D* and *ε* [19–22,24,25].

The UDEDM model presented in Fig. 3(c), were to analyze this model considers the values of *D*, *ε*, *σ*, and energy density (*u*) [19–25,33]. The slope and intercept values for the UDEDM model in Tables 1 and 2 for the values *D*, *ε*, *σ*, and *u*. The *D*, *ε*, and *σ* UDEDM models confirm the correlation between UDM and USDM models in the WH method, which shows the same value [19,20]. The value *u* changes with the addition of AC [19–22,24,25] as the effect of *ε* and *σ* in the UDM and USDM models.

Fig. 4 shows the Size-Strain Plot Method (SSP). The SSP method is an analysis method by correcting the results of the WH method [19–25,33]. The slope and intercept values for Fig. 4 of the SSP method are given in Tables 1 and 2 for the *D*, *ε*, *σ*, and *u*. We get the SSP method's different small values for the structural properties with the Scherrer method and the WH method as can be seen clearly SSP data more reliable compared with another methods due to the all physical parameter for SSP including in the calculation. At high concentration of carbon (20 % AC) shows some data are spreading at low $(d_{hkl})^2\beta_{hkl}cos\theta$ indicated that, the C atoms from AC may play an essential role in active site in bonding together to form heterogeneous nucleation. The process of shifting from homogeneous nucleation at low concentration of AC (10 %) to heterogeneous nucleation when the amount of AC increases up to 20 % AC is not fully understand which still needs for further study.

3.2. Optical properties

The optical properties of the composite from the quantitative analysis of FTIR spectroscopy are determined. We used the FTIR spectra of composite CuO with 10 % AC and 20 % AC from our previous published paper in Ref. [6]. We focus on the wavenumbers $350-1500$ cm^{-1} due to inorganic groups' vibrating modes at $350-600$ cm^{-1} and the aromatic plane bending at $950-1250$ cm^{-1} [6–11]. At this wavenumbers, Cu-O-C and Cu-O bonds are formed from inorganic groups and C–H bonds from aromatic plane bending, as shown in Fig. 5(a). These regions are explicit explained the interaction between CuO and AC.

The Cu-O-C bond is responsible for photocatalytic activity by the generation of electron and hole pairs [2,15]. The electron at the valance band absorbing the energy from the photo (photon) for excitation to the conduction band and remain hole at the valence band [2,13]. Both of the charge (electron and hole) move to the surface and fall in the pore of AC. Inside the pore the electron will be adsorbed the oxygen atoms and produce O2*- radicals and the hole disturbs the H_2O molecule to produce H + and OH* radicals. These radical atoms which going to disturbing the pollutant atoms and the final product is H_2O and CO_2 [13,40].

The optical properties are determined from the quantitative analysis using the Kramers-Kronig (K-K) relation [22,35–39] in FT-IR spectra. This method usually applied in electron spectroscopy spectra [41–47] but used infra-red spectroscopy spectra in this study. First step; converting the transmittance $T(\omega)$ to reflectance [22,35,37] by converting transmittance to reflectance $R(\omega)$ using the equation $T(\omega) =$

$(1 - R(\omega))^2/(1 - (R(\omega))^2)$, for $R(\omega) \ll$ then the equation become $R(\omega) = 1 - (T(\omega))^{1/2}$ to form reflectance. The complex refractive indexes can be present as $\hat{n}(\omega) = n(\omega) + k(\omega)$, where *n* (*ω*) is the refractive index for the real part and *k* (*ω*) is the extinction coefficient for the imaginary part [25,33,35], *n* and *k* represented in Eqs. (3) and (4). Where *φ* (*ω*) is the phase change between the incident and reflected signals for a particular wavenumber (*ω*) by using the Eq. (5) [22,35,37]. The K-K relation, Eq. (5) modified to become Eq. (6) [22,36,37] as follows:

$$n(\omega) = \frac{1 - R(\omega)}{1 + R(\omega) - 2\sqrt{R(\omega)}\cos\varphi(\omega)} \quad (3)$$

$$k(\omega) = \frac{2\sqrt{R(\omega)}\sin\varphi(\omega)}{1 + R(\omega) - 2\sqrt{R(\omega)}\cos\varphi(\omega)} \quad (4)$$

$$\varphi(\omega) = -\frac{\omega}{\pi}\int_0^\infty \frac{lnR(w^{'}) - lnR(\omega)}{\omega^{'2} - \omega^2} \quad (5)$$

$$\varphi(\omega_j) = -\frac{4\omega_j}{\pi} x \, \Delta\omega \, x \sum_i \frac{\ln(\sqrt{R(\omega)})}{\omega_i^2 - \omega_j^2} \quad (6)$$

Eq. (6) can be explained that *j* is wavenumbers. If *j* is odd number, then *i* is *2,4,6,8, …, j-1, j + 1* and if j is even number, then *i* is *1,3,5,7, …., j-1, j + 1, …* $\Delta\omega = \omega_{i+1} - \omega_i$ [28–31]. The results of this analysis are in Fig. 5(b) where *n* and *k* crosses occur to transverse optical (*To*) and longitudinal optical (*Lo*) phonon vibrations, which show of the wavenumbers shifted due to the addition of AC as shown in Table 3. The value of *To* has increased, and *Lo* was decreasing indicated the nucleation at the active site, which successfully modified structural properties consistent with the phenomena by the quantitative analysis of XRD spectra in the previous section.

Fig. 5(c) shows the dielectric function (*ε₁* dan *ε₂*) from the quantitative analysis of FT-IR spectra, where *ε₁* is the real part and *ε₂* is the imaginary part of the dielectric function presented in the function $(\bar{\varepsilon}(\omega) = \varepsilon_1(\omega) + i\varepsilon_2(\omega))$, were described in Eqs. (7) and (8) [35–38]:

$$\varepsilon_1(\omega) = n^2(\omega) - k^2(\omega) \quad (7)$$

$$\varepsilon_2(\omega) = 2n(\omega)k(\omega) \quad (8)$$

The prominent peak of *ε₁* and *ε₂* are shown in Fig. 5(c) was a shift to the lower wavenumber position from the CuO at 568.60 cm^{-1} to composite 10 % at 563.74 cm^{-1}, and 20 % AC at 562.94 cm^{-1}, indicated successfully AC in modified the electronic properties, probably in the form of heterogeneous nucleation. The intensity changed with the addition of AC, where *ε₂* has decreased linearly. The AC successfully play an essential role in improving surface adsorption energy of the molecules. It also charges and the active site in strong bonding to form heterogeneous nucleation, as confirmed by the XRD spectra in Fig. 1. The pore of the AC useful for absorbing the energy and the charge in the process of photocatalyst and also use as a linker in bonding together with Cu and O atom which dominated by strong covalent bond. Photocatalyst process, first, the electron at the valance band move to the conduction band when they are absorbing the energy from the photo (photon) and remain hole at the valence band [2,13]. The second process, the electron and hole capture by the pore, the electron adsorbed the oxygen atoms and produce O2*- radicals and the hole disturbs the H_2O molecule and produce H + and OH* radicals. The third, radical atoms are going to disturbing the pollutant atoms resulting the final product is H_2O and CO_2 [13,40].

3.3. Particle size from TEM method

Particle size analysis using Transmission Electron Microscopy (TEM) is a method to confirm the crystallite size from the quantitative analysis of XRD spectra [19–22,34–39,41–48]. In this research, we measuring
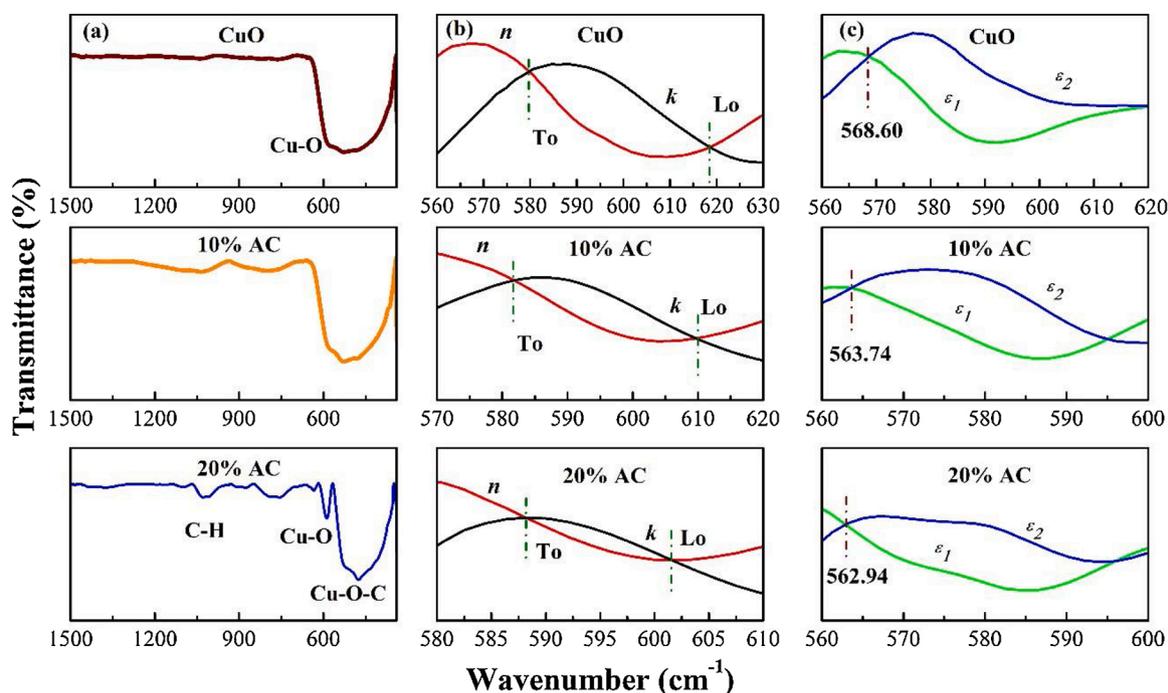
Fig. 5. (a). FT-IR spectrum, (b). refractive index (n) and extinction coefficient (k), To is transversal optical phonon mode and Lo is longitudinal optical phonon mode. (c). real (ε_1) and imaginary parts (ε_2) of the dielectric function for CuO and composite CuO-AC (10 % AC and 20 % AC).

Table 3

Transverse optical phonon (*To*) and longitudinal optical phonon (*Lo*) from the quantitative analysis of FT-IR spectra in Fig. 7. The rate constant (k_r) and correlation coefficient values (R^2) of CuO and composite CuO-AC (10 % AC and 20 % AC) from degradation analysis in Fig. 10.

Sample	*To*	*Lo*	Rate constant ((k_r) min^{-1})	Correlation coefficient values (R^2)
CuO	579.78	618.52	0.004	0.863
10 % AC	581.64	610.01	0.015	0.974
20 % AC	588.15	601.52	0.024	0.998

the TEM for composites 10 % AC and 20 % AC. Fig. 6(a) shows the TEM micrograph and the particle size distribution correspondingly in Fig. 6 (b).

The particle size's D_{TEM} average diameter is 32.5 nm and 37.5 nm for the composite 10 % AC and 20 % AC, respectively. Interestingly, from these results, the D_{TEM} is linearity with the SSP result, which shows the effect of strain on the particle size based on the SSP method [19–22,24, 34]. The particle size from the TEM method is comparing with the Scherrer method, WH method, and the SSP method, as shown in Table 4. It is found that the changes in the values D, ε, σ, and u in each model are the effect of the electronic properties by the interactions between CuO and AC indicated that the AC was successfully in modification [6,13,16, 18–20,26].

3.4. Photocatalytic performance

Fig. 7(a) shows the absorption of UV–vis spectra of CuO and composites CuO-AC for photocatalytic performance using methylene blue as a pollutant. It can be seen that along with the addition of AC, the material's absorption increases, so only the short time needed to produce harmless pollutants. The change value in absorption from CuO to composite 20 % AC only 90 min to be perfectly harmless due to surface adsorption energy increase due to the active site is strong bonding to form heterogeneous nucleation. Fig. 7(b) shows the percentage of

degradation. The percentage of degradation of methylene blue calculated by using the equation; D (%) $= \frac{C_0 - C_t}{C_0}$ x 100%, where D (%) is the percentage of degradation, C_0 is the control absorbance (before irradiation), and C_t is the absorbance after time t [1–5,12–15,49–53]. The best degradation percentage is for the composite 20 % AC, which reached 87.87 % with 90 min compared with CuO material, which only degraded 38.41 % for 120 min. XRD spectra confirm that, the FWHM changes for two diffraction peaks at 32.17° and 35.72° indicated, the carbon addition could demonstrate the successfully modified the surface of CuO which useful for increasing the efficiency of photocatalytic degradation [4,12,13,50,53].

The photocatalytic performance will be observing from the rate constant of degradation (k_r), where the high value of k_r indicated good performance [3–5,13,52,53]. The carbon-related materials, in this case the AC will act both: electron-acceptor and electron-transport materials which will facilitate the migration of photoinduced electrons and suppression the charge recombination to enhance the photo-catalytic performance [14,43,54,55]. In Ref [40,52,53,56,57]. was reported that, the magnetic materials by co-doped with carbon-based materials will significant increases the photo-catalytic activity due to suppression of the recombination of electron-hole pairs. The best photo-catalytic performance of CuO-AC composite is 20 % AC indicated by 87.87 % degraded only for 90 min radiation. The k_r value calculated by using the equation $\ln \left(\frac{C_0}{C_t} \right) = k_r t$, where C_0 is the initial absorbance (before irradiation), and C_t is the absorbance after time t, t is the reaction time, and k_r is the rate constant of degradation [12–15]. The value of correlation coefficient (R^2) of the close to 1 show good photocatalytic performance [2,13, 14,54]. Table 3 shows the value of k_r and R^2 from Fig. 8(a), k_r increases with the addition 20 % AC in composites, and R^2 also increases to close to 1, indicating potential photocatalytic performance [13,15,52,55]. Kinetic curves of photocatalytic degradations presented in Fig. 8(b), where the rate kinetic approaches 0 with the addition of AC increase, this indeed confirms that the correlation between k_r and R^2 (Fig. 8) to the potential photocatalytic degradation efficiency, as presented in Fig. 7. The crystallite size increase and the *Lo* and *To* shifts ordered with increasing the amount of AC indicated that the electronic properties
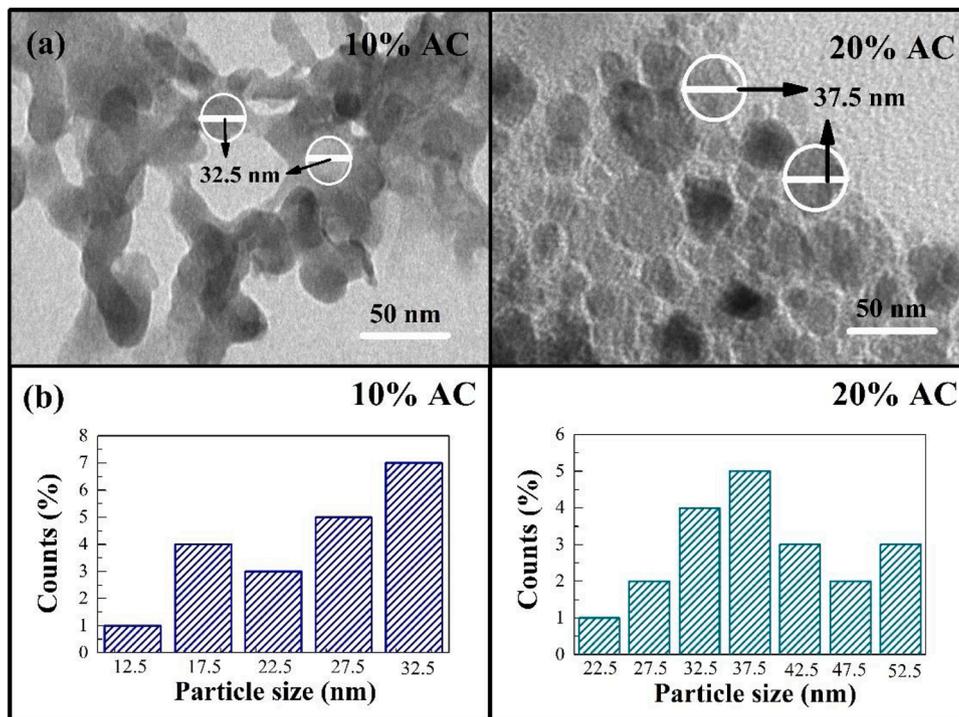
Fig. 6. (a) TEM image and (b) particle size distribution for composite CuO-AC (10 % AC and 20 % AC).
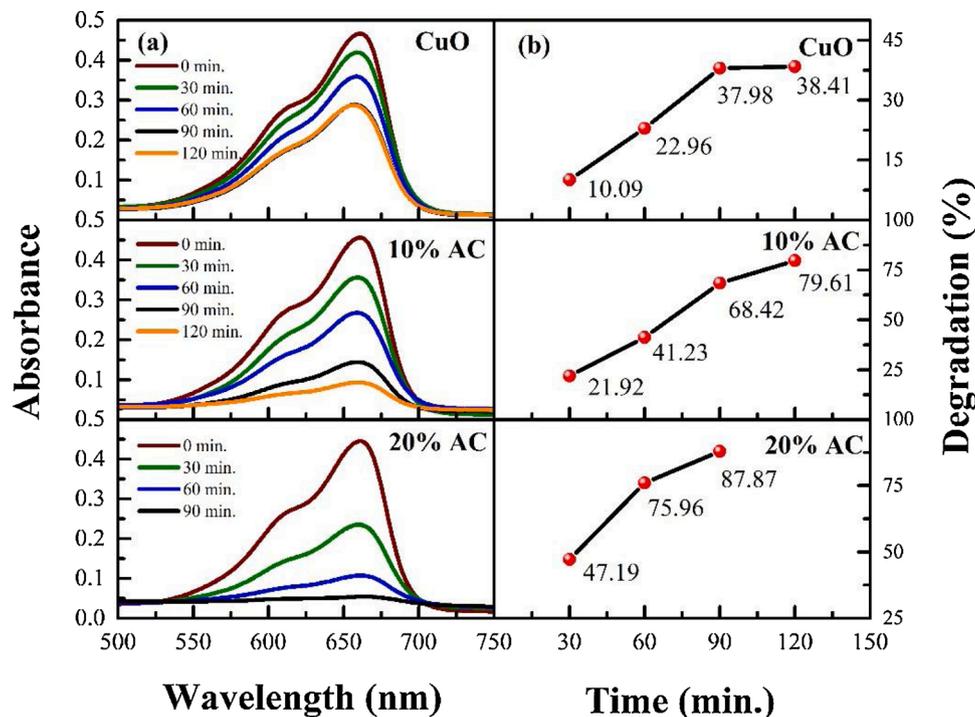
Fig. 7. (a) UV–vis absorption spectra and (b) Percentage of degradation for CuO and composite CuO-AC (10 % AC and 20 % AC).

were modified. It confirmed by the enhanced coefficient correlation value (R^2) and subsequently increased photocatalytic performance.

Fig. 9 shows relation between structural and optical properties with the composites performance for EM wave and photocatalytic. The reflection loss (RL) taken from our previous published [6] compares with photocatalytic output. For optical phonon vibration mode in the form of Lo shows decreases with increasing the amount of AC but *To* is vice versa. The crystallite size (D) for composites shows increases with

increasing the amount of AC, probably due to the amorphous phase of AC covering the atoms of Cu and form heterogeneous nucleation. The degradation performance shows an increase of 87.87 %, similar for RL with the thickness 2 mm taken from Ref. [6] shows potentials to attenuate the EM wave up to 99 % indicated by the RL below -20 dB. The crystallite size (D) increase and optical phonon vibration shifted (Lo decrease and To increase) and close each other high contributed in increasing the percentage of degradation up to 87.87 % in 90 min and

Table 4
Crystallite Size of CuO and composite CuO-AC (10 % AC and 20 % AC) from different method and Particle size from TEM method for comparison.

Sample	Scherrer Method	Williamson-Hall Method			Size-Strain Plot Method	TEM Method
		UDM	USDM	UDEDM		
	D (nm)	D (nm)	D (nm)	D (nm)	D (nm)	D_{TEM} (nm)
CuO	20.81	20.38	20.38	20.38	25.12	–
10 % AC	20.60	20.03	20.03	20.03	21.47	32.5
20 % AC	21.96	23.01	23.01	23.01	27.29	37.5

attenuate EM wave 99 % for composite with 20 % AC. The second and the third cycle of composite CuO-AC for 25 % AC in the process of photocatalysist shows degradation up to 85.6 % and 83.5 % in 90 min, respectively. These results indicated that the composites CuO-AC is high potentials multifunction materials which the excellent photocatalytic applications and very good absorber EM waves which can attenuate up to 99 %.

4. Conclusion

In this study, the relation between the structural and optical properties in supporting the photocatalytic performance and absorber of EMI of composite CuO-AC successfully demonstrated. The crystallite size (D) obtained from the XRD spectra affected by values of ε, σ, and u of CuO and composites CuO-AC based on the Scherrer method, WH method, and SSP method. The Optical phonon vibration (Lo and To) obtained from the optical properties that quantitative analysis of FTIR spectra shows close each other the wavenumber due to AC's addition. The shifted cross point of the function from 568.60 cm^{-1} for CuO, 563.74 cm^{-1} for 10 % AC, and 562.94 cm^{-1} for 20 % AC also confirm the successfully modified electronic properties of composite CuO-AC. The particle size confirmed based on TEM results shows linear relation with crystallite size from the quantitative analysis by various XRD spectra model. The crystallite size (D) for composites CuO-AC increases with increasing the amount of AC due to the hexagonal structure of AC covering the Cu atoms to form heterogeneous nucleation. The degradation performance shows an increase of 87.87 %, similar for RL with the thickness 2 mm shows potentials to attenuate the EM wave up to 99 % indicated by the RL below -20 dB. The k_r increases with increasing the amount of AC up to 20 % AC and the value of R^2 also increased and close to 1, indicating a high
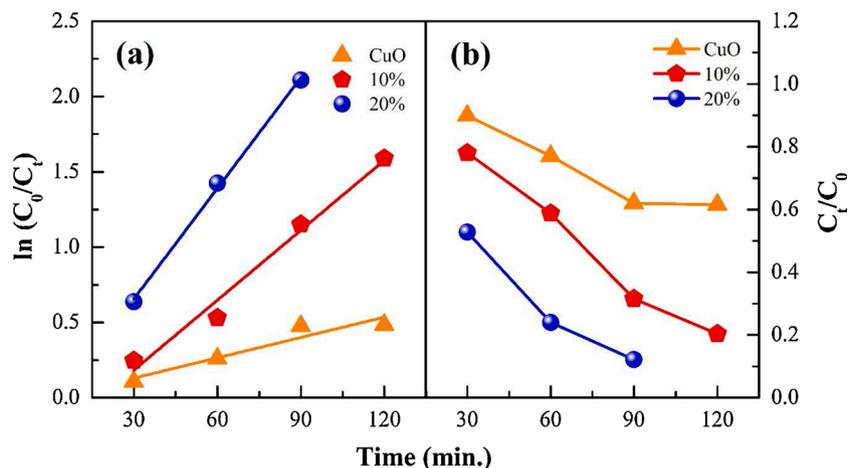
Fig. 8. (a) Photocatalytic performance and (b) Kinetic curve of photocatalytic degradations for CuO and composite CuO-AC (10 % AC and 20 % AC).
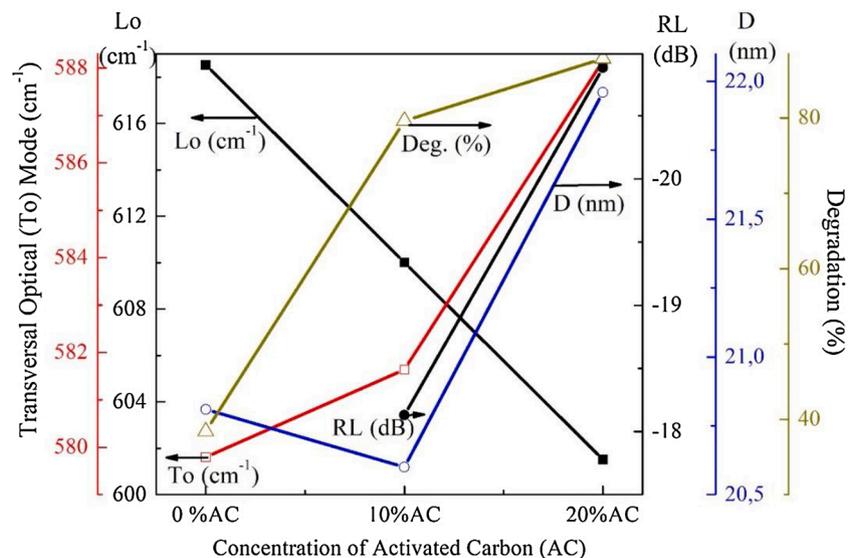
Fig. 9. The relation between structural properties and optical properties with the photocatalytic performance and the ability in attenuate the electromagnetic wave. The RL data taken from Ref. [6] for comparison the photocatalytic performance to find the best composition.

potential of composite CuO-AC for photocatalytic application. The crystallite size (D) increase and optical phonon vibration shifted (Lo decrease and To increase) and close each other high contributed in increasing the percentage of degradation up to 87.87 % in 90 min and attenuate EM wave 99 % for composite with 20 % AC.

Author contribution statement

Sultan Ilyas, contributed to the conception of the study, analysis, and manuscript preparation; Heryanto, performed the data analysis and wrote the manuscript; Dahlang Tahir perform the analysis with constructive discussion, paper proof-reading, and response to reviewer.

Declaration of Competing Interest

None.

Acknowledgments

Appendix A. Supplementary data

Supplementary material related to this article can be found, in the online version, at doi:https://doi.org/10.1016/j.jece.2020.104670.

References

[1] P.K. Labhane, S.H. Sonawane, G.H. Sonawane, S.P. Patil, V.R. Huse, Influence of Mg doping on ZnO nanoparticles decorated on graphene oxide (GO) crumpled paper like sheet and its high photo catalytic performance under sunlight, J. Phys. Chem. Solids 114 (2018) 71–82, https://doi.org/10.1016/j.jpcs.2017.11.017.

[2] G. Zhao, R. Guo, Z. Mo, P. Zhang, B. Wang, X. Zhu, Synthesis of graphene/Fe_3O_4/NiO magnetic nanocomposites and its application in photocatalytic degradation the organic pollutants in wastewater, J. Porous. Mater. 22 (2015) 1245–1253, https://doi.org/10.1007/s10934-015-0002-1.

[3] M.S. Gohari, A.H. Yangjeh, M. Abitorabi, A. Rouhi, Magnetically separable nanocomposites based on ZnO and their applications in photocatalytic processes: a review, Crit. Rev. Environ. Sci. Technol. (2018), https://doi.org/10.1080/10643389.2018.1487227. ISSN: 1064-3389 (Print) 1547-6537 (Online).

[4] A. Akhundi, A.H. Yangjeh, M. Abitorabi, S.R. Pouran, Review on photocatalytic conversion of carbon dioxide to value-added compounds and renewable fuels by graphitic carbon nitride-based photocatalysts, Catal. Rev. (2019), https://doi.org/10.1080/01614940.2019.1654224. ISSN: 0161-4940 (Print) 1520-5703 (Online).

[5] M. Pirhashemi, A.H. Yangjeh, S.R. Pouran, Review on the criteria anticipated for the fabrication of highly efficient ZnO-based visible-light-driven photocatalysts, J. Ind. Eng. Chem. 62 (2018) 1–25, https://doi.org/10.1016/j.jiec.2018.01.012.

[6] D. Tahir, S. Ilyas, B. Abdullah, B. Armynah, K. Kim, H.J. Kang, Modification in electronic, structural, and magnetic properties based on composition of composites Copper (II) Oxide (CuO) and Carbonaceous material, Mater. Res. Express 6 (2019) 035705, https://doi.org/10.1088/2053-1591/aaf7da.

[7] P. Chand, M. Manisha, P. Kumar, Effect of precursors medium on structural, optical and dielectric properties of CuO nastructures, Optik 156 (2018) 743–753, https://doi.org/10.1016/j.ijleo.2017.12.029.

[8] D.A. Svintsitskiy, T.Y. Kardash, O.A. Stonkus, E.M. Slavinskaya, A.I. Stadnichenko, S.V. Koscheev, A.P. Chupakhin, A.I. Boronin, In situ XRD, XPS, TEM, and TPR study of highly active in CO oxidation CuO nanopowder, J. Phys. Chem. C 117 (2013) 14588–14599, https://doi.org/10.1021/jp403339r.

[9] C. Oruc, A. Altundal, Structural and dielectric properties of CuO nanoparticles, Ceram. Int. 43 (14) (2017) 10708–10714, https://doi.org/10.1016/j.ceramint.2017.05.006.

[10] V.S. De Souza, H.O. Da Frota, E.A. Sanches, Polyaniline CuO hybrid nanocomposite with enhanced electrical conductivity, J. Mol. Struct. 1153 (2018) 20–27, https://doi.org/10.1016/j.molstruc.2017.09.084.

[11] S.K. Kuanr, S. Nayak, K.S. Babu, Ni dependent structural, optical and electrical properties of CuO nanostructures, Mater. Sci. Semicond. Process. 71 (2017) 268–274, https://doi.org/10.1016/j.mssp.2017.08.012.

[12] Y. Cheng, J. Cao, Y. Li, Z. Li, H. Zhao, G. Ji, Y. Du, The outside-in approach to construct Fe_3O_4 nanocrystals/mesoporous carbon hollow spheres core–shell hybrids toward microwave absorption, ACS Sustain. Chem. Eng. 6 (2018) 1427–1435, https://doi.org/10.1021/acssuschemeng.7b03846.

[13] S. Ilyas, B. Abdullah, D. Tahir, Enhancement of absorbing frequency and photo-catalytic performance by temperature treatment of composites Fe_3O_4-AC nanoparticle, Adv. Powder Technol. (2020), https://doi.org/10.1016/j.apt.2019.11.007.

[14] S.S. Agjekandy, A.H. Yangjeh, Ultrasonic-assisted preparation of novel ternary $ZnO/AgI/Ag_2CrO_4$ nanocomposites as visible-light-driven photocatalysts with excellent activity, Mater. Sci. Semicond. Process. 44 (2016) 48–56, https://doi.org/10.1016/j.mssp.2015.12.025.

[15] J. Qin, X. Zhang, C. Yang, M. Cao, M. Ma, R. Liu, ZnO microspheres-reduced graphene oxide nanocomposite for photocatalytic degradation of methylene blue dye, Appl. Surf. Sci. 392 (2017) 196–203, https://doi.org/10.1016/j.apsusc.2016.09.043.

[16] B. Abdullah, S. Ilyas, D. Tahir, Nanocomposites Fe/activated carbon/PVA for microwave absorber: synthesis and characterization, . 6 (2018) 9823263, https://doi.org/10.1155/2018/9823263.

[17] B. Abdullah, A. Nisyah, S. Ilyas, D. Tahir, Structural properties and bonding characteristics of honeycomb structure of composite $ZnMnO_2$ and activated carbon, J. Appl. Biomater. Funct. Mater. 17 (2019) 1–6, https://doi.org/10.1177/2280800818820185.

[18] D. Tahir, S. Ilyas, B. Abdullah, B. Armynah, H.J. Kang, Electronic properties of composite iron (II, III) oxide (Fe_3O_4) carbonaceous absorber materials by electron spectroscopy, J. Electron Spectros. Relat. Phenomena 229 (2018) 47–51, https://doi.org/10.1016/j.elspec.2018.09.008.

[19] S. Ilyas, B. Heryanto, D..Tahir Abdullah, X-ray diffraction analysis of nanocomposite Fe_3O_4/activated carbon by Williamson-Hall and size-strain plot methods, Nano-structures Nano-objects 20 (2019) 100396, https://doi.org/10.1016/j.nanoso.2019.100396.

[20] B. Heryanto, D..Tahir Abdullah, Mahdalia, Quantitative analysis of X-ray diffraction spectra for determine structural properties and deformation energy of Al, Cu and Si, J. Phys. Conf. Ser. 1317 (2019) 012052, https://doi.org/10.1088/1742-6596/1317/1/012052.

[21] B. Heryanto, D. Abdullah, Tahir, Determination of Binding Energy For Cu and Cu_2O Based X-Ray Diffraction Spectrum, J. Phys. Conf. Ser. 979 (2018) 012055, https://doi.org/10.1088/1742-6596/979/1/012055.

[22] S. Suryani, Rusdaeni Heryanto, A.N. Fahri, D. Tahir, Quantitative analysis of diffraction and infra-red spectra of composite cement/$BaSO_4$/Fe_3O_4 for determining correlation between attenuation coefficient, structural and optical properties, Ceram. Int. 46 (11) (2020) 18601–18607, https://doi.org/10.1016/j.ceramint.2020.04.170.

[23] A. Khorsand Zak, W.H. Abd, M.E. Majid, Abrishami and Ramin Yousefi, X-ray analysis of ZnO nanoparticles by Williamson-Hall and size-strain plot methods, Solid State Sci. 13 (2011) 251–256, https://doi.org/10.1016/j.solidstatesciences.2010.11.024.

[24] B.R. Kumar, B. Hymavathi, X-ray peak profile analysis of solid-state sintered alumina doped zinc oxide ceramic by Williamson-Hall and size-strain plot methods, J. Asian Ceram. Soc. 5 (2017) 94–103, https://doi.org/10.1016/j.jascer.2017.02.001.

[25] M.N. Siddique, T. Ali, A. Ahmed, P. Tripathi, Enhanced electrical and thermal properties of pure and Ni substituted ZnO Nanoparticles, Nano-structures Nano-objects 16 (2018) 156–166, https://doi.org/10.1016/j.nanoso.2018.06.001.

[26] Q. Zhang, K. Zhang, D. Xu, G. Yang, H. Huang, F. Nie, C. Liu, S. Yang, CuO nanostructures: Synthesis, characterization, growth mechanisms, fundamental properties, and applications, Prog. Mater. Sci. 60 (2014) 208–337, https://doi.org/10.1016/j.pmatsci.2013.09.003.

[27] H. Siddiqui, M.S. Qureshi, F.Z. Haque, Biosynthesis of flower-shaped CuO nanostructures and their photocatalytic and antibacterial activities, Nano-micro Lett. 12 (2020) 29, https://doi.org/10.1007/s40820-019-0357-y.

[28] H. Siddiqui, M. Shrivastava, M.R. Parra, P. Pandey, S. Ayaz, M.S. Qureshi, The effect of La^{3+} ion doping on the crystallographic, optical and electronic properties of CuO nanorods, Mater. Lett. 229 (2018) 225–228, https://doi.org/10.1016/j.matlet.2018.07.029.

[29] P. Chand, A. Gaur, A. Kumar, U.K. Gaur, Structural and optical study of Li doped CuO thin films on Si (1 0 0) substrate deposited by pulsed laser deposition, Appl. Surf. Sci. 307 (2014) 280–286, https://doi.org/10.1016/j.apsusc.2014.04.027.

[30] H. Siddiqui, M.R. Parra, M.M. Malik, F.Z. Haque, Structural and optical properties of Li substituted CuO nanoparticles, Opt. Quantum Electron. 50 (2018) 260, https://doi.org/10.1007/s11082-018-1527-8.

[31] H. Siddiqui, M.S. Qureshi, F.Z. Haque, Alkali metals doped $Cu_{0.95}X_{0.05}O$ (X = Li, Na, and K) nanoparticles : facile synthesis, structural, optical properties and solar cell application, Mater. Lett. 275 (2020) 128090, https://doi.org/10.1016/j.matlet.2020.128090.

[32] H. Siddiqui, M.R. Parra, P. Pandey, M.S. Qureshi, F.Z. Haque, Performance evaluation of optimized leaf-shaped two-dimension (2D) potassium doped CuO nanostructures with enhanced structural, optical and electronic properties, Ceram. Int. 46 (2020) 20404–20414, https://doi.org/10.1016/j.ceramint.2020.05.131.

[33] Hendri Heryanto, B. Abdullah, D. Tahir, Analysis of Structure Properties of X-ray diffraction for composite copper-activated carbon by modified Williamson-Hall and size-strain plotting methods, J. Phys. Conf. Ser. 1080 (2018) 012007, https://doi.org/10.1088/1742-6596/1080/1/012007.

[34] A. Gholizadeh, A Comparative study of physical properties in Fe_3O_4 nanoparticles prepared by coprecipitation and citrate methods, J. Am. Ceram. Soc. (2017) 1–12, https://doi.org/10.1111/jace.14896.

[35] Gh.H. Khorrami, A.K. Zak, A. Kompany, R. yousefi, Optical and structural properties of X-doped (X = Mn, Mg, and Zn) PZT nanoparticles by Kramers–Kronig and size strain plot methods, Ceram. Int. 38 (2012) 5683–5690, https://doi.org/10.1016/j.ceramint.2012.04.022.

[36] R. Zamiri, H.M. Chenari, H.F. Moafi, Mehdi Shabani, S.A. Salehizadeh, A. Rebelo, J. Suresh Kumar, M.P.F. Graça, M.J. Soares, J.M.F. Ferreira, Ba-doped ZnO nanostructure: X-ray line analysis and optical properties in visible and low

frequency infrared, Ceram. Int. 42 (11) (2016) 12860–12867, https://doi.org/10.1016/j.ceramint.2016.05.051.

[37] M. Ghasemifard, E. Fathi, M. Ghamari, The effect of Fe^{3+}-doped on structure and optical properties of mesoporous Al_2O_3/SiO_2 composite, Mater. Sci. Semicond. Process. 42 (2016) 349–353, https://doi.org/10.1016/j.mssp.2015.11.001.

[38] M. Ghasemifard, S.M. Hosseini, Gh.H. Khorrami, Synthesis and structure of PMN–PT ceramic nanopowder free from pyrochlore phase, Ceram. Int. 35 (2009) 2899–2905, https://doi.org/10.1016/j.ceramint.2009.03.036.

[39] S. Ilyas, D. Tahir, Suarni, B. Abdullah, S. Fatimah, Structural and bonding properties of honeycomb structure of composite nanoparticles Fe_3O_4 and activated carbon, J. Phys. Conf. Series 1317 (2019) 012058, https://doi.org/10.1088/1742-6596/1317/1/012058.

[40] Z. Xie, Y. Feng, F. Wang, D. Chen, Q. Zhang, Y. Zeng, W. Lv, G. Liu, Construction of carbon dots modified MoO_3/g-C_3N_4 Z-scheme photocatalyst with enhanced visible-light photocatalytic activity for the degradation of tetracycline, Appl. Catal. B 229 (2018) 96–104, https://doi.org/10.1016/j.apcatb.2018.02.011.

[41] M.J. Iqbal, N. Yaqub, B. Sepiol, B. Ismail, A study of the influence of crystallite size on the electrical and magnetic properties of $CuFe_2O_4$, Mater. Res. Bull. 46 (2011) 1837–1842, https://doi.org/10.1016/j.materresbull.2011.07.036.

[42] D. Tahir, J. Kraaer, S. Tougaard, Electronic and optical properties of Fe, Pd, and Ti studied by reflection electron energy loss spectroscopy, J. Appl. Phys. 115 (2014) 243508, https://doi.org/10.1063/1.4885876.

[43] D. Tahir, S.K. Oh, H.J. Kang, S. Tougaard, Quantitative analysis of reflection electron energy loss spectra to determine electronic and optical properties of Fe-Ni alloy thin films, J. Electron Spectrosc. Relat. Phenom. 206 (2016) 6–18, https://doi.org/10.1016/j.elspec.2015.11.005.

[44] D. Tahir, S.K. Oh, H.J. Kang, S. Tougaard, Composition Dependence of Dielectric and Optical Properties of Hf-Zr-Silicate Thin Films Grown on Si (100) by Atomic Layer Deposition, Thin Solid Films 616 (2016) 425–430, https://doi.org/10.1016/j.tsf.2016.09.001.

[45] D. Tahir, H.L. Kwon, H.C. Shin, S.K. Oh, H.J. Kang, S. Heo, J.G. Chung, J.C. Lee, S. Tougaard, Electronic and optical properties of Al_2O_3/SiO_2 thin films grown on Si substrate, J. Phys. D Appl. Phys. 43 (2010) 255301, https://doi.org/10.1088/0022-3727/43/25/255301.

[46] D. Tahir, S. Tougaard, Electronic and optical properties of selected polymers studied by reflection electron energy loss spectroscopy, J. Appl. Phys. 111 (2012) 054101, https://doi.org/10.1063/1.3688327.

[47] D. Tahir, E.H. Choi, Y.J. Cho, S.K. Oh, H.J. Kang, H. Jin, S. Heo, J.G. Chung, J. C. Lee, S. Tougaard, Electronic and optical properties of La-aluminate dielectric thin films on Si (100), Surf. Interface Anal. 42 (10-11) (2010) 1566–1569, https://doi.org/10.1002/sia.3590.

[48] Y.K. Lahsmin, D. Tahir, B. Abdullah, S. Ilyas, I. Mutmainna, Synthesis of carbon nanosphere at low temperatures based on bamboo Fiber, Mater. Sci. Forum 966 (2019) 163–168, https://doi.org/10.4028/www.scientific.net/MSF.966.163.

[49] S. Sood, S. Kumar, A. Umar, A. Kaur, S.K. Mehta, S.K. Kansal, TiO_2 quantum dots for the photocatalytic degradation of indigo carmine dye, J. Alloys. Compd. 650 (2015) 193–198, https://doi.org/10.1016/j.jallcom.2015.07.164.

[50] M. Mousavi, A.H. Yangjeh, S.R. Pouran, Review on magnetically separable graphitic carbon nitride-based nanocomposites as promising visible-light-driven photocatalysts, J. Mater. Sci.: Mater. Electron 29 (2018) 1719–1747, https://doi.org/10.1007/s10854-017-8166-x.

[51] B. Priya, P. Shandilya, P. Raizada, P. Thakur, N. Singh, P. Singh, Photocatalytic mineralization and degradation kinetics of ampicillin and oxytetracycline antibiotics using graphene sand composite and chitosan supported biocl, J. Mol. Catal. A Chem. 423 (2016) 400–413, https://doi.org/10.1016/j.molcata.2016.07.043.

[52] P. Raizada, J. Kumari, P. Shandilya, R. Dhiman, V.P. Singh, P. Singh, Magnetically retrievable Bi_2WO_6/Fe_3O_4 immobilized on graphene sand composite for investigation of photocatalytic mineralization of oxytetracycline and ampicillin, Process. Saf. Environ. Prot. 106 (2017) 104–116, https://doi.org/10.1016/j.psep.2016.12.012.

[53] P. Raizada, A. Sudhaik, P. Singh, P. Shandilya, A.K. Saini, V.K. Gupta, J.-H. Lim, H. Jung, A.H. Bandegharaei, Fabrication of Ag_3VO_4 decorated phosphorus and sulphur co-doped graphitic carbon nitride as a high-dispersed photocatalyst for phenol mineralization and E. Coli disinfection, Sep. Purif. Technol. 212 (2019) 887–900, https://doi.org/10.1016/j.seppur.2018.12.007.

[54] K. Ravichandran, N. Chidhambaram, T. Arun, S. Velmathi, S. Gobalakrishnan, Realizing cost-effective ZnO:Sr nanoparticles for improved photocatalytic and antibacterial activities, RSC Adv. 6 (2016) 67575–67585, https://doi.org/10.1039/C6RA08697G.

[55] S.S. Agjekandy, A.H. Yangjeh, Ultrasonic-assisted preparation of novel ternary $ZnO/AgI/Ag_2CrO_4$ nanocomposites as visible-light-driven photocatalysts with excellent activity, Mater. Sci. Semicond. Process. 44 (2016) 48–56, https://doi.org/10.1016/j.mssp.2015.12.025.

[56] W. GuO, Y. Yang, Y. Guo, Y. Jia, H. Liu, Y. Guo, Self-assembled hierarchical $Bi12TiO20$–graphene nanoarchitectures with excellent simulated sunlight photocatalytic activity, Phys. Chem. Chem. Phys. 16 (2014) 2705–2714, https://doi.org/10.1039/C3CP53070A.

[57] A. Sudhaik, P. Raizada, P. Shandilya, P. Singh, Magnetically recoverable graphitic carbon nitride and $NiFe2O4$ based magnetic photocatalyst for degradation of oxytetracycline antibiotic in simulated wastewater under solar light, J. Environ. Chem. Eng. (2018).